2D and 3D inversion of MT data from the continental collision zone in the Pamir and Tien Shan, Central Asia

P. Sass*, O. Ritter*, A. Rybin**, and V. Batalev**
*Helmholtz Centre Potsdam GFZ, German Research Centre for Geosciences
**Research Station of the Russian Academy of Sciences, Bishkek, Kyrgyzstan

1 Introduction

A disputed question in geodynamics is the mode of deformation and ultimate fate of lithosphere in collisional mountain building. The Pamir – Tien Shan region in Central Asia may be the best location on Earth to observe lithospheric deformation during orogeny in progress. This mountain range and high plateau formed at the tip of the western Indian promontory through Cenozoic shortening of a magnitude similar to the adjacent Himalaya-Tibet system. The Pamir – Tien Shan orogenic belt hosts some of the deepest active intra-continental subduction zones on Earth and absorbs the highest strain rate over the shortest distance that is manifested in the India–Asia collision zone. The multi-disciplinary Tien Shan – Pamir Geodynamic Program (TIPAGE) combines numerical geodynamic modeling, structural geology, geo-thermochronology and petrology with multiple passive source geophysical experiments, i.e. a seismic and a magnetotelluric (MT) survey in Kyrgyzstan and Tajikistan, predominantly along a 350 km long N-S profile. The MT method is sensitive to electrically conductive regions in the crust and mantle, which often imply the presence of fluids. Hence, with MT we address crucial topics such as crustal flow and fluid release by continental subduction processes.

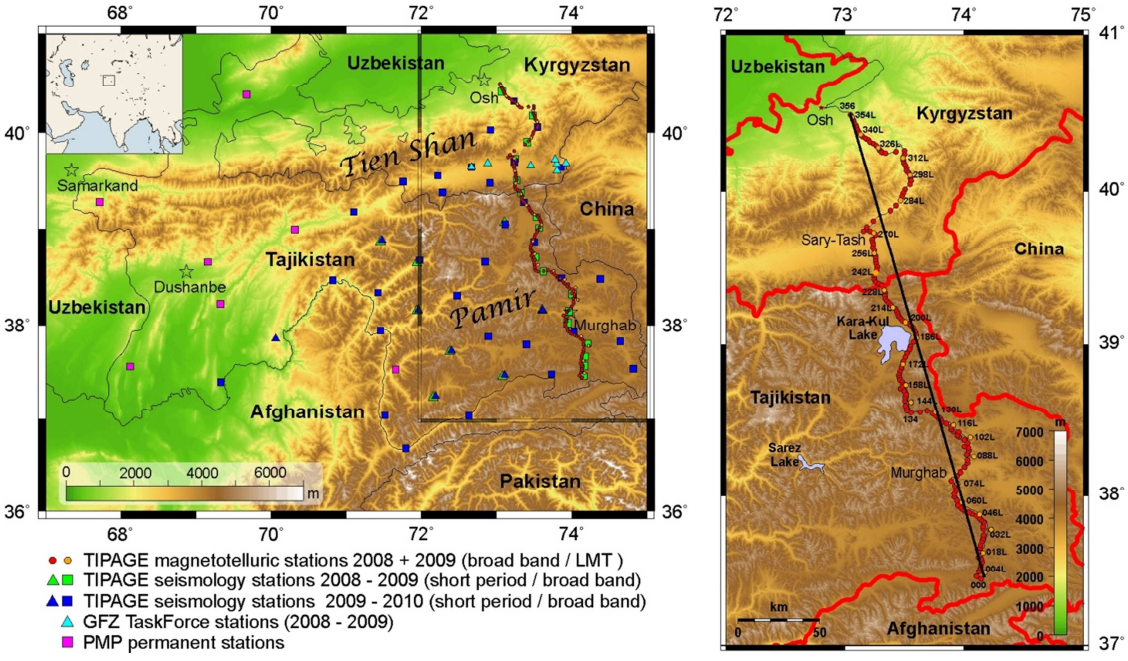

Figure 1: Overview map with all TIPAGE stations (MT + seismology, left) and the location the TIPAGE MT profile (right). Labeled sites mark positions of combined long period (LMT) and broad band (BB) stations, dots show BB-only stations.

Figure 1 shows two overview maps of the TIPAGE area. The left map shows all TIPAGE stations including seismological sites, the right map presents only the magnetotelluric profile

area. MT data was recorded in two field campaigns in 2008 and 2009 along a 340 km long corridor from southern Tajikistan to Osh in Kyrgyzstan across the Pamir Plateau and southern Tien Shan mountain ranges. In total there are 178 MT stations, whereof 26 combine broad band (10^{-3} s - 10^{3} s) and long period (up to 10^{4} s) recordings.

2 Data Analysis and Results

2.1 Data Processing

At each of the MT stations we recorded five channel electromagnetic data: two horizontal magnetic and electric fields and the vertical magnetic field. We used the robust, remote-reference EMERALD data processing package (Ritter 1998, Weckmann 2005, Krings 2007) to obtain apparent resistivity, phase and induction vector data. Particularly in the sparsely populated northern Pamir region, data quality was excellent; figure 2 shows two examples of transfer functions from sites 052 on the Pamir plateau and site 228 which is close to the Tajik – Kyrgyz border. Curves of both sites were obtained after applying standard single-site processing (for station locations, see figure 1).

Nevertheless, many of the TIPAGE MT stations from Kyrgyzstan are affected by anthropogenic electromagnetic noise and needed to be processed in a more sophisticated and individual way in order to improve the data quality. Figure 3 shows a representative example of noise-affected data of the station 288 from a more densely populated Tien Shan mountain valley in the northern profile part. The standard single site processing yields highly scattered and noisy data curves especially for the periods of the ”dead band” between 1 s and 10 s (Figure 3, left diagram). The quality of this and many other station data could be improved using the remote reference processing technique whereat the undisturbed source fields at a remote site which is recording simultaneously are used to clean the signal. The right diagram of figure 3 was gained after a remote reference processing of site 288, using station 222 as the remote site. The data quality improves significantly.

Apparent resistivity and phase data of all sites are plotted as pseudo-sections in figure 4, in which the amplitude and phase values are color-coded. For the pseudo-section presentation, the data are already rotated according to the geo-electric strike (see below) into TE (currents perpendicular to strike) and TM modes (currents parallel to strike). As a preparatory measure for 2D inversion, some of the more noisy data points were masked; we also removed some data points exhibiting phase values >90° (at long periods), as they are indication for the presence of 3D structures.

The vertical magnetic transfer functions can be used to investigate lateral variations of conductivity. Often they are visualized as induction vectors. In the Wiese convention (Wiese 1962), they tend to point away from good conducting zones. This convention was used in figures 2 and 3. Maps views of the real and imaginary parts of induction vectors at different periods are shown in figure 5.

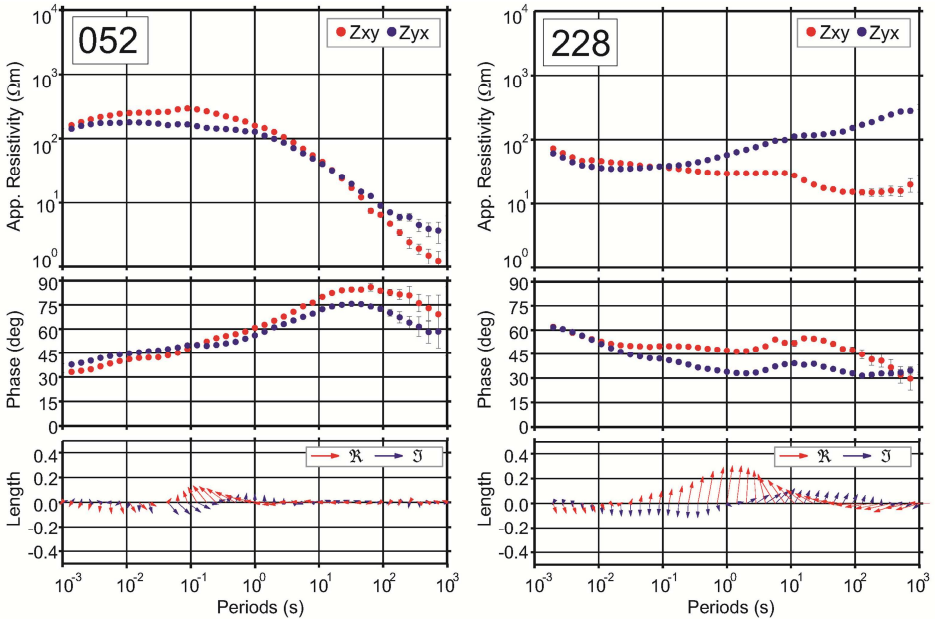

Figure 2: Examples of high-quality curves of apparent resistivity, phases and induction vectors of station 052 (left diagram) and station 228 (right diagram). For station location, see figure 1.

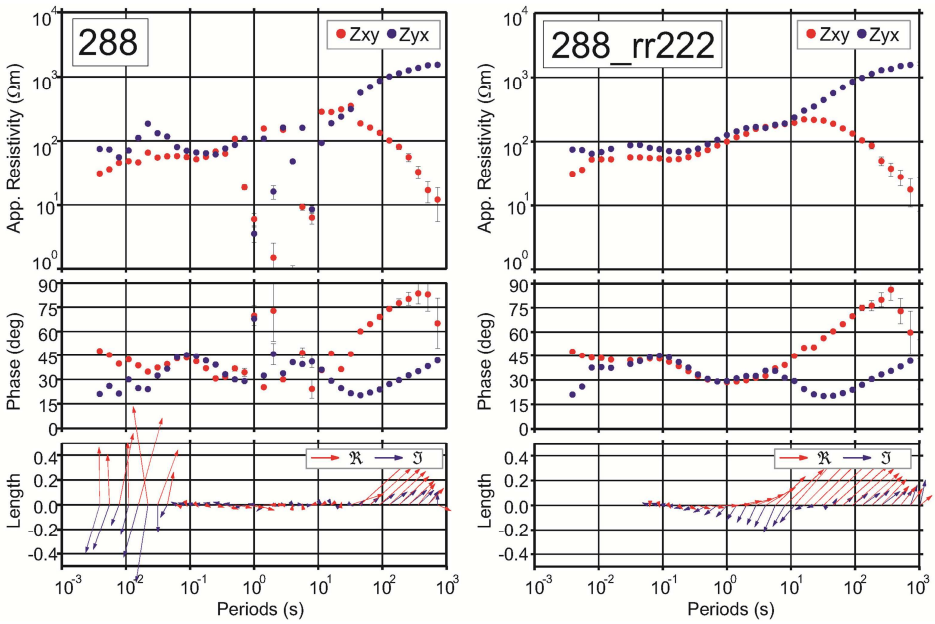

Figure 3: Apparent resistivity, phases and induction vectors of station 288 after the standard single site processing (left diagram) and the remote reference processing using station 222 as the remote site (right diagram).

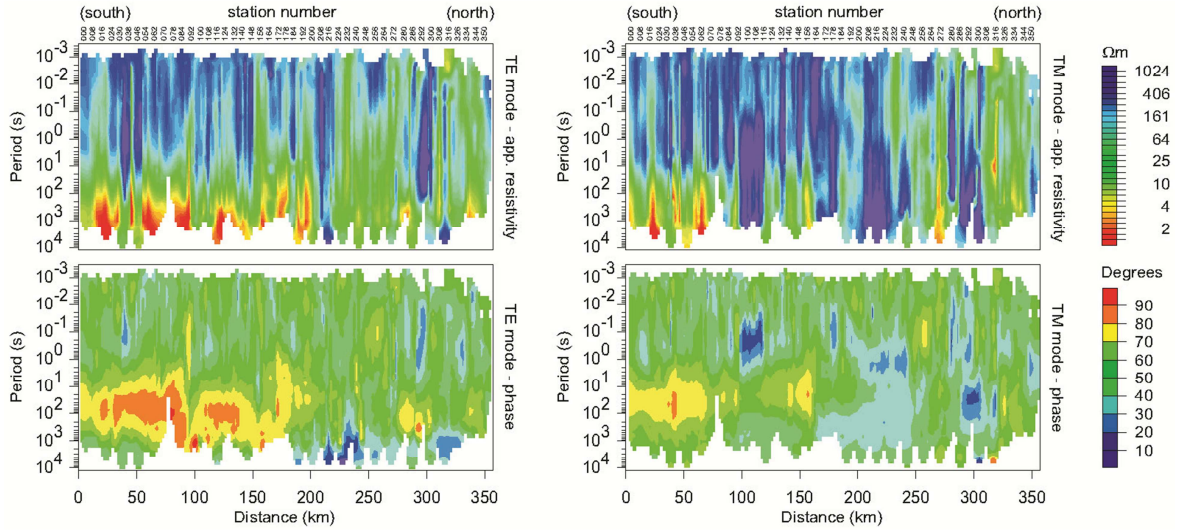

Figure 4: Pseudosections of apparent resistivity and phases of all stations, TE mode (left) and TM mode (right). Noisy data points and phases > 90° are removed.

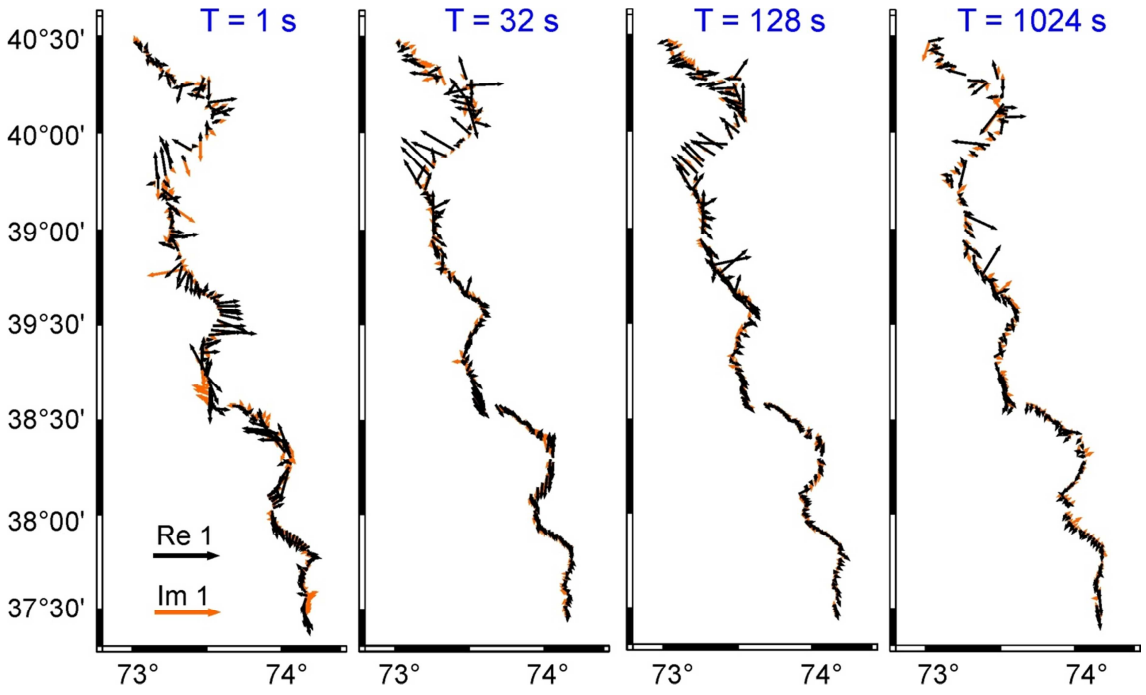

Figure 5: Maps of induction vectors (real and imaginary part) of each station at different periods from T = 1 s (left) to T = 1024 s (right). The arrows are plotted according to the Wiese convention (Wiese 1962) and tend to point away from good conducting zones.

2.2 Strike Detection

We performed a strike direction analysis after Becken and Burkhard (2004). The obtained rose diagrams include cardinal points and are shown in figures 6 and 7. The gray shaded areas, which point in a certain direction of the diagram, represent stations with a certain direction of main current flow at the considered frequencies. The bigger the length of the gray area in a certain direction, the more stations have a dominating current flow in this direction. The principal 90° ambiguity of the impedance tensor strike analysis results in the cross-shaped diagrams and can be resolved by using the induction vectors (figure 5). In figure 6, the left diagram was obtained using only the short period data between 0.0001 s and 1 s which penetrates only the upper crust (depth less than 10 km). The average strike direction is predominantly W-E. When analyzing the longer periods (10 s - 10000 s) we obtain a dominating strike direction of approximately -15° to -20° N (figure 6, right diagram), which shows the dominating strike in middle to lower crustal levels. This picture is generally consistent with the predominant geological and tectonic trend in the area and justifies 2–dimensional inversion of the data. However, a more detailed analysis in figure 7 provides information about the spatial distribution of the strike directions at different periods and for different profile parts. This compilation exhibits larger variability in the strike directions. At the shortest periods, the strike directions scatter. This could hint at the influence of local 3D structures but could also be due to local 1D condition for which strike directions are undetermined. The strike at longer periods is generally more uniform along the profile, though some scattering is present.

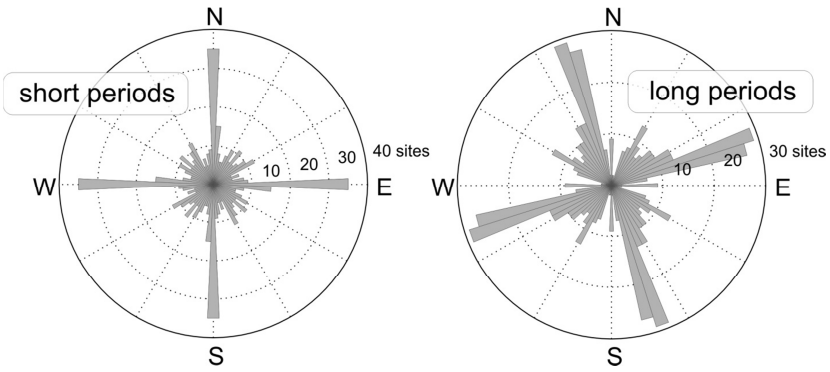

Figure 6: Electrical strike direction analysis, including all stations and a period range 0.0001 s - 1 s (left diagram) and 10 s - 10000 s (right diagram). The diagrams show the number of stations with a certain direction of the main current flow (Becken & Burkhard, 2004). Longer periods include deeper layers.

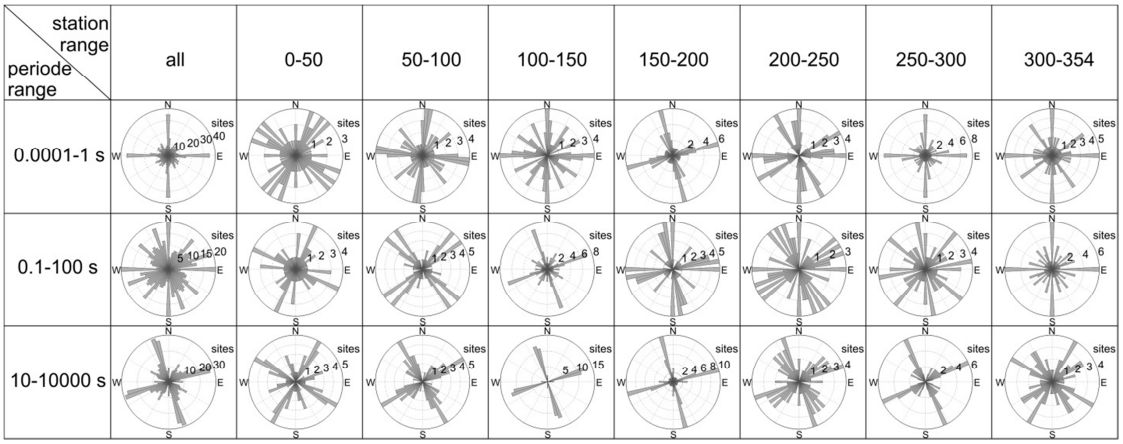

Figure 7: Electrical strike direction analysis for different periods (rows) and station ranges (columns).

A non-dimensional rotationally invariant parameter to characterize the complexity of subsurface structures is the skew of the impedance tensor defined by Swift (1967) or Bahr (1988). A 1D or 2D conductivity distribution results in a skew value of 0, whereas greater values indicate the presence of 3D structures. Practically, a value of 0.2 to 0.3 is still considered as small and generally consistent with 2D assumptions. Pseudosections of the skewness in Figure 8 show values below 0.3 for most stations and periods. Skew values > 0.4 occur at stations 60 to 90 for longer periods, where we also observed phases >90°. Large skew values towards the northern end of the profile are likely caused by anthropogenic noise.

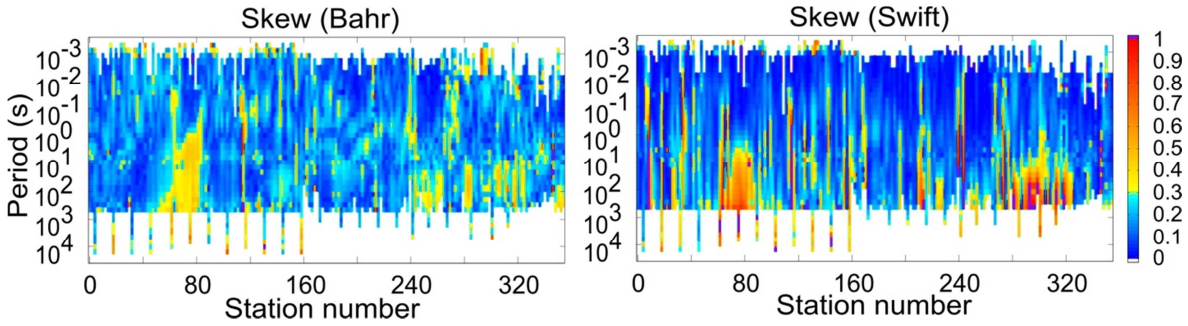

Figure 8: Pseudosection of the skewness in the definition of Swift (left) and Bahr (right). Blue colors indicate skew values below 0.3, which are considered to be compatible with 2D assumption (Swift 1967, Bahr 1988).

2.3 2D Inversion

To solve the 2D magnetotelluric inverse problem we used an algorithm based on a regularized, nonlinear conjugate gradients (NLCG) scheme (Rodie and Mackie, 2001), implemented in the WinGLink software package (version 2.20.09).

After rotation of the data by -105° (see prev. section and figure 6) the x-direction of the data, which prior to the rotation pointed northwards, shows now to WSW-direction, parallel to the dominating strike. For the 2D inversion, all stations locations were projected onto the profile line marked in Figure 1 (right hand side).

To probe at least some parts of the solution space we varied systematically some of the inversion parameters, including starting model, frequency range, error floors and data weighting. An important aspect of this particular inversion scheme is finding the most appropriate smoothness (regularization) factor. Plotting the roughness vs. the RMS of inversion results with different settings of the smoothing parameter τ yields a Pareto front, which is shown in Figure 9. The best value of τ, as an optimum trade-off between coherent structures and data misfit, is found close to the kink of the Pareto front; here we choose τ = 30.

The result of the 2D inversion can be found in Figure 10 together with the topography and major tectonic features. To obtain this model we used only the longer period data between 0.1 s and 10000 s. Due to grid size restrictions, we had problems fitting the shorter periods, so the upper 5 to 10 km are not resolved in this model.

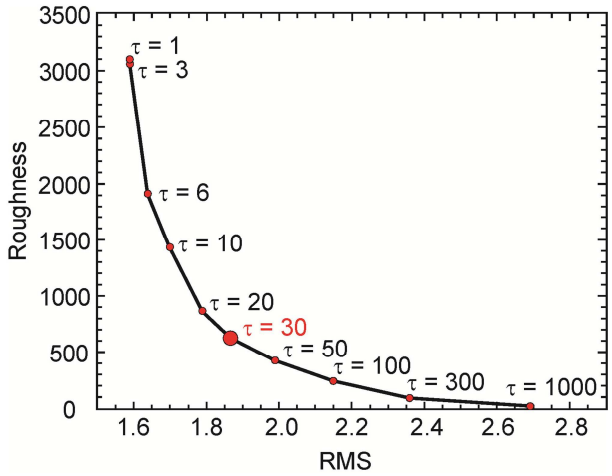

Figure 9: Pareto front: roughness vs. RMS for a range of smoothing parameters τ; here, a reasonable choice is τ = 30.

For the inversion we concentrated on fitting the phase curves rather than the static-shift-affected apparent resistivity curves by setting large error floors for the TE-mode apparent resistivity (see Figure 10 for the inversion settings). The fit of both phase curves and the TM mode resistivity is fairly good, resulting in a total RMS of 1.87. Detailed diagrams of the RMS errors for every component are given in figure 11. The RMS values were calculated according to

$$RMS(d) = \sqrt{\frac{1}{N_d} \cdot \frac{1}{(err_d)^2} \cdot \sum_{n=1}^{N_d} \left[\ln(d_{n,obs}) - \ln(d_{n,calc})\right]^2} \ ,$$

where d indicates a data component (e. g. certain data mode and certain station), N_d the number of data points for component d (e. g. number of periods), err_d the estimated error for the component d, $d_{n,obs}$ and $d_{n,calc}$ are the observed (measured) and calculated (model response) data points, respectively. The very low RMS values for ρ_{TE} in figure 11 are caused by the extremely high pre-set error floor values. The lowermost diagram of figure 11 shows a comparison of RMS given by WinGLink and the total values calculated manually. The bias which is present at the RMS values of WinGLink and our calculation varies between different models, but the WinGlink RMS are always lower than ours. We are not sure how the RMS is calculated in WinGLink, but the absolute RMS value is less important than the general trend of the data misfit distribution, which is in good agreement in the two RMS curves.

The models reveal a generally resistive upper crust for the Pamir plateau and several regions of high conductivity at lower crustal levels. Below the Pamir plateau we observe prominent conductive structures at depths of approx. 20 km – 40 km. The absolute values for resistivity and depth ranges of these conductors are in the same range as observed from the Tibetan plateau which were interpreted as zones of lower crustal flow (Bai et al., 2010).

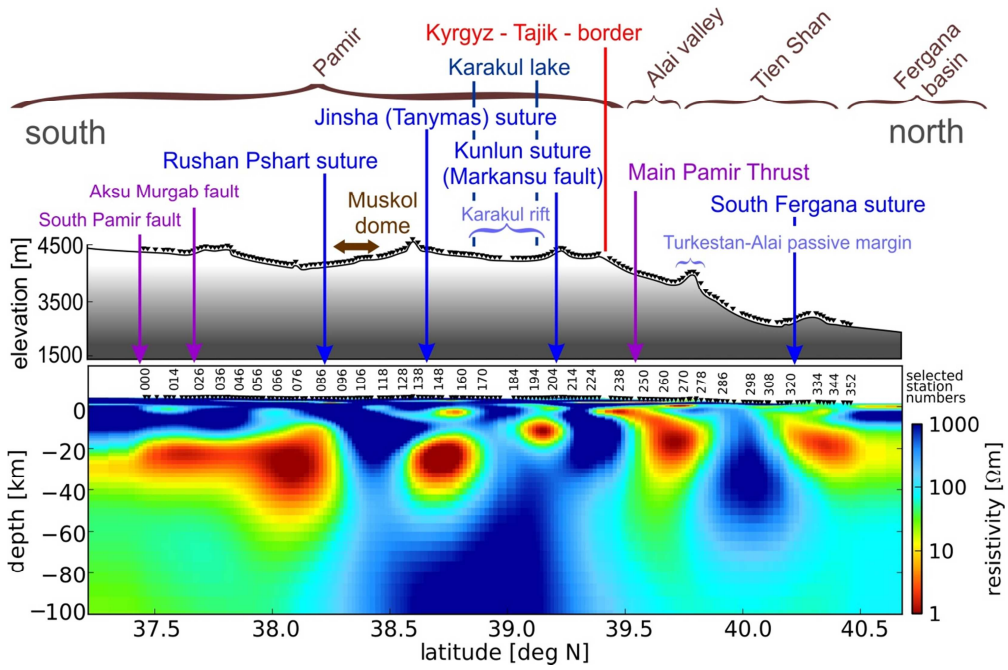

Figure 10: 2D inversion result, truncated at a depth of 100 km. Also shown are the topography and the main tectonic features (Schwab & Ratschbacher, 2004 and Robinson, 2007). The model was obtained using the 2D inversion algorithm of Rodie and Mackie (2001), convergence was achieved with 400 iterations. Settings (WinGLink): joint inversion for TE + TM + Hz mode, 156 x 176 cells, τ = 30, R_{start} = 100 Ωm, weighting: α = β = 1, H = V = 500, error floors: ρ_{TE} = 10000%, ϕ_{TE} =1.5°, ρ_{TM} = 30%, ϕ_{TM} =1.5°, T_{yz} =0.05. RMS = 1.87.

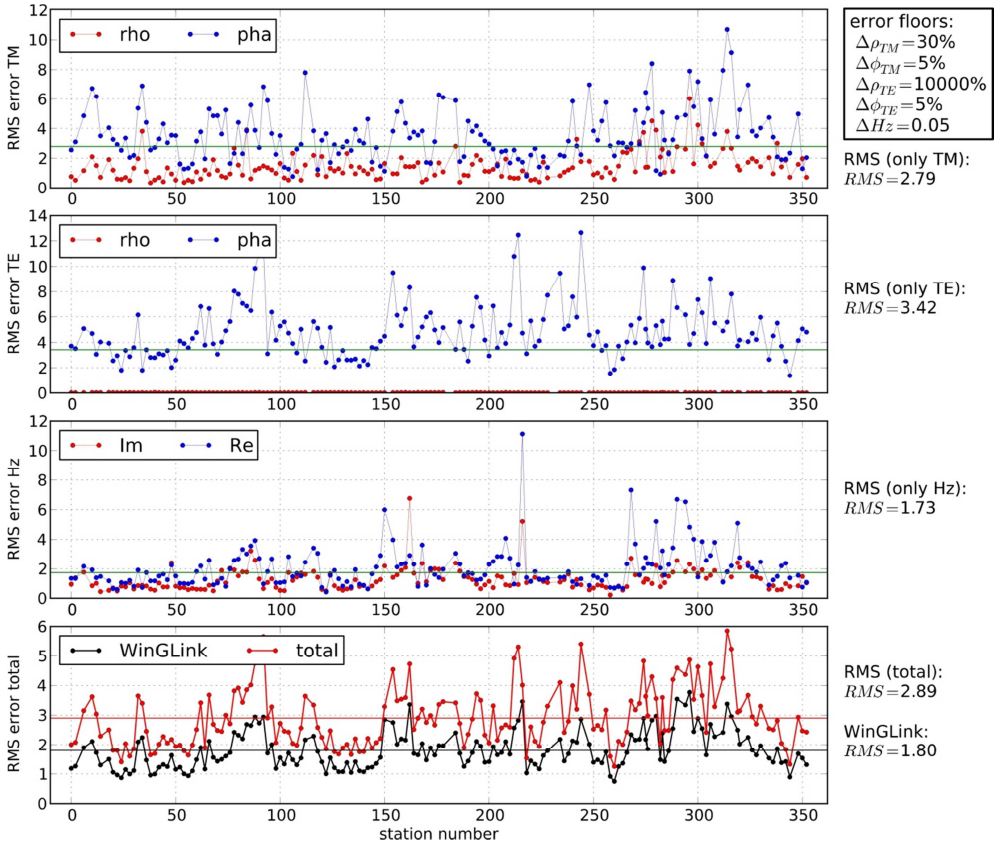

Figure 11: RMS error for each data mode and every station of the 2D model in figure 10. Error floors used for calculation of the RMS values are shown in the box. The lowermost diagram shows a comparison of RMS given by WinGLink and the total values calculated manually.

2.4 3D Inversion

Preliminary 3D inversion was performed using the parallelized version of ModEM (Egbert & Kelbert 2012). Figure 12 exhibits smaller scale resistive features in the upper layers but also some prominent conductors at approximately 20 km depth. The slices also show that the inversion modifies only cells in the vicinity of the profile. The area affected increases with increasing induction range (larger periods). Comparison of a slice through the 3D model with the corresponding 2D model (Figure 13) clearly shows that the main conductivity features are visible in both models. This is remarkable considering that the 3D model was calculated using only a subset of stations and a different grid. While these preliminary 3D results confirm our 2D inversion model, more 3D inversion will be a major part of our future work.

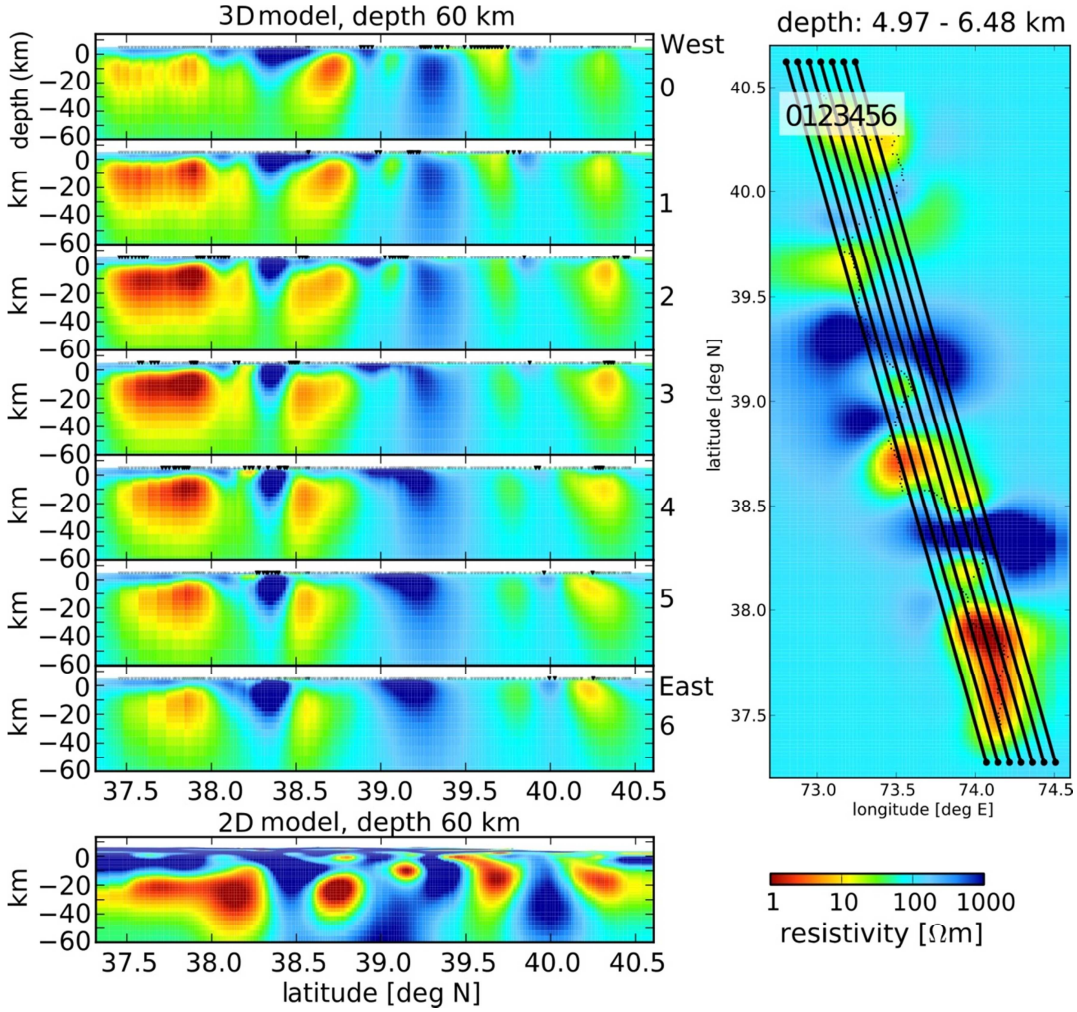

Figure 12: Vertical slices through a 3D model to a depth of 60 km. Location of the slices are shown in a map view on the right hand side. Section 0 is the westernmost slice, section 6 is the easternmost slice. For comparison, the 2D model from figure 10 is plotted below the 3D model slices. Most of the major features appear in both inversion images.

2.5 Topography Influence

Topography can have an influence on magnetotelluric data and inversion results. Electromagnetic field lines are “compressed” by concave topographies and “stretched” by convex structures (Fox 1980). Consequently, a higher potential difference of the electric field over a certain distance is measured in valleys in comparison to measurements on ridges, which causes valley to appear as too restive valleys and ridges appear as too conductive. As the TIPAGE area is dominated by mountains, it is crucial to check the influence of the topography on the inversion results. Therefore, we constructed a 3D model with layers reproducing the real topography and a homogeneous conductivity distribution in the rest of the model space. We used an algorithm for computing the magnetotelluric response of three-dimensional earth models, which is implemented in the 3D-forward-module of the WinGLink package (Mackie et al., 1993). We calculated the model response of this 3D topography model at places of our receiver stations. Taking this response as station data we inverted it in the 2D scheme. The result is displayed in figure 13. All conductivity structures in the inversion originate only from topography. The starting model was a 100 Ωm half space. Maximum differences between inversion result and the starting model (100 Ωm) are approximately ± 80 Ωm. Hence, the influence of topography on the real data, were resistivity varies over more than four orders of magnitude, is minor. Please note the different color scales in figure 13 and in the model plots in figures 10 and 12. In order to compare the influence of topography on the model with the influence of some subsurface resistivity distribution, in figure 14 the same color scale is used as in the model plots.

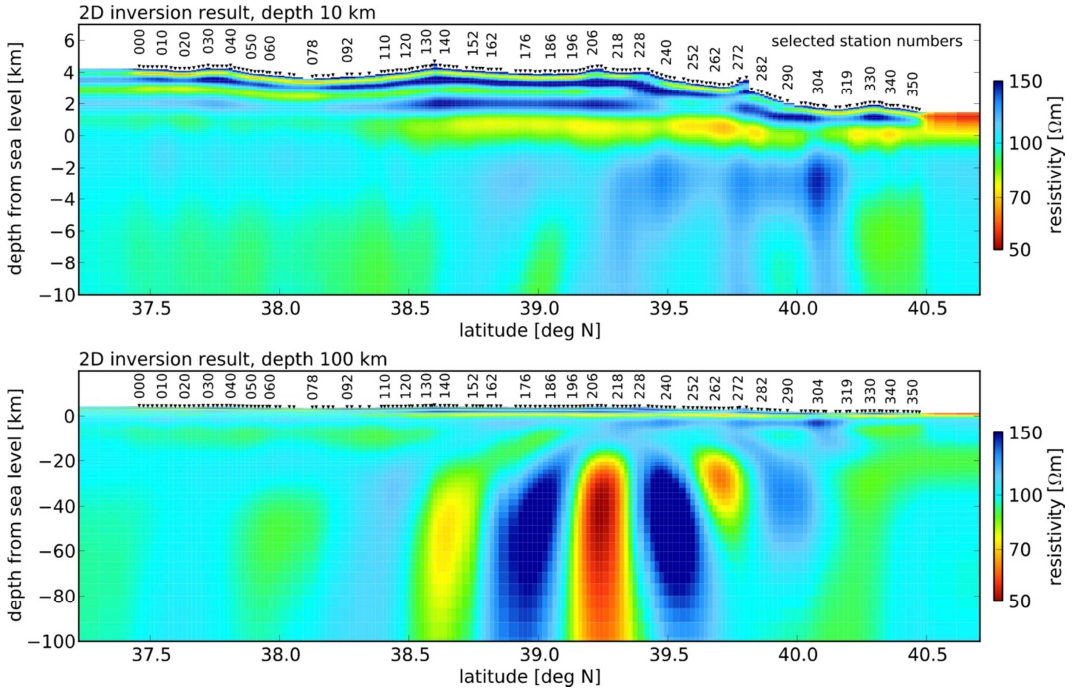

Figure 13: Topography influence on TIPAGE MT data. Upper plot: shallow layers down to -10 km depth below NN, lower plot: deep layers 0-100 km depth. The models were obtained after a 2D inversion of a 3D forward response of the modeled topography at places of MT stations. The color scale is chosen to amplify changes from a 100 Ωm half space.

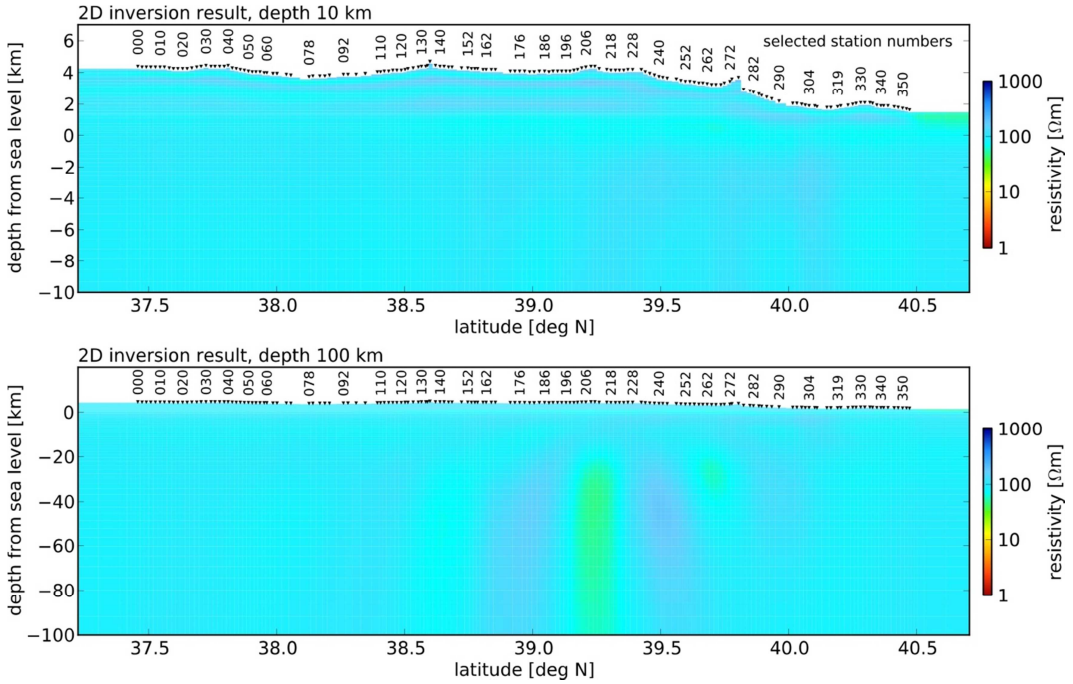

Figure 14: Similar as in figure 13, but now using the same color scale as in figures 10 and 12. The artificial subsurface features created by the inversion are due to topography. However, the contrasts are rather weak and have little influence on the inversion result.

Acknowledgements

The MT field team: Employees and students of the International Research Center, Russian Academy of Sciences, Bishkek and from Germany: D. Brändlein, X. Chen, T. Krings, A. Nube, M. Schüler, K. Tietze, C. Twardzik and G. Willkommen.

Dr. V. E. Minaev, Dr. N. Radjabov, Dr. I. Oimahmadov, Prof. A. R. Faiziev: Institute of Geology, Academy of Sciences of the Republic of Tajikistan, Dushanbe.

Dr. B. Moldobekov, Prof. H. Echtler, Dr. A. Mikolaichuk: Central Asian Institute for Applied Geosciences, Bishkek.

Dr. S. K. Negmatullaev: PMP International / Seismic Monitoring Network in Tajikistan, Dushanbe.
Prof. L. Ratschbacher: University of Freiberg, Germany and all other German colleagues participating in this project.

We very gratefully acknowledge substantial funding which we received from the DFG and GFZ. Seismic and magnetotelluric instruments were provided by the GFZ Geophysical Instrument Pool (GIPP).

References

Bahr, K. (1988), Interpretation of the magnetotelluric impedance tensor: regional induction and local telluric distortion. J. Geophys., 62:119–127.

Bai, D. et al. (2010), Crustal deformation of the eastern Tibetan plateau revealed by magnetotelluric imaging, Nature Geoscience 3, 358 – 362

Becken, M. and Burkhardt, H. (2004), An ellipticity criterion in magnetotelluric tensor analysis. Geophysical Journal International, 159: 69–82.

Egbert, G. and Kelbert, A. (2012), Computational Recipes for EM Inverse Problems. Geophysical Journal International, 189, 1.

Fox, R.C., Hohmann, G.W., Killpack, T.J., and Rijo, L. (1980), Topographic effects in resistivity and induced-polarisation surveys. Geophysics, 45, 75–93.

Krings, T. (2007), The influence of Robust Statistics, Remote Reference, and Horizontal Magnetic Transfer Functions on data processing in Magnetotellurics. Diploma thesis, Westfälische Wilhelms-Universität Münster and GeoForschungsZentrum Potsdam.

Mackie, R. L., Madden, T. R. , and Wannamaker, P.E. (1993), Three-dimensional magnetotelluric modeling using difference equations; theory and comparisons to integral equation solutions. Geophysics 58(2): 215-226

Ritter, O., Junge, A. and Dawes, G. (1998), New equipment and processing for magnetotelluric remote reference observations. Geophysical Journal International, 132: 535–548.

Robinson A. C. et al. (2007), Cenozoic evolution of the eastern Pamir: Implications for strain-accommodation mechanisms at the western end of the Himalayan-Tibetan orogen, GSA Bulletin, v. 119, no. 7/8, p. 882–896

Rodi, W., Mackie, R. (2001), Nonlinear conjugate gradients algorithm for 2-D magnetotelluric inversion, Geophysics 66: 174-187

Schwab, M., et al. (2004), Assembly of the Pamirs: Age and origin of magmatic belts from the southern Tien Shan to the southern Pamirs and their relation to Tibet, Tectonics, 23, TC4002

Swift, C. M. (1967), A Magnetotelluric Investigation of an Electrical Conductivity Anomaly in the Southwestern United States. PhD thesis, Massachusetts Institute of Technology, Cambridge, Massachusetts, USA.

Weckmann, U., Magunia, A., and Ritter, O. (2005), Effective noise separation for magnetotelluric single site data processing using a frequency domain selection scheme. Geophysical Journal International, 161: 635–652.

Wiese, H. (1962), Geomagnetische Tiefentellurik Teil ii: Die Streichrichtung der Untergrundstrukturen des elektrischenWiderstandes, erschlossen aus geomagnetischen Variationen, Pure and Applied Geophysics, 52: 83–103